Progress in Physics of Applied Materials
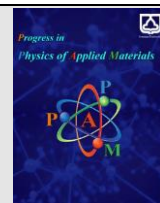
Hydrothermal synthesis of WO$_3$ nanorods: pH adjustment stage, additive comparison and photocatalysis activities

Behnam Purhadi[a], Mohaddeseh Jamali[a], Zohreh Bahrami[b], Fatemeh Shariatmadar Tehrani[a]*

[a] *Faculty of Physics, Semnan University, P.O. Box: 35195363, Semnan, Iran*
[b] *Faculty of New Sciences and Technologies, Semnan University, P.O. Box: 3513119111, Semnan, Iran*

A R T I C L E   I N F O

A B S T R A C T

Additives as surfactant can affect the structural, morphological, and optical properties of WO$_3$ nanostructures. However, it is important to find optimum amount of additive for obtaining the best nanostructure of WO$_3$. Therefore, the effect of oxalic acid (C$_2$H$_2$O$_4$) and potassium sulfate (K$_2$SO$_4$) concentration as organic and inorganic additives were studied in this work. Also, the effect of pH adjustment stage (before/after oxalic acid addition) in the synthesis process was investigated for the first time. The WO$_3$ nanostructures were characterized by X-ray powder diffraction (XRD), Raman scattering, field emission scanning electron microscopy (FESEM) and diffuse reflection spectroscopy (DRS). In addition, the photocatalysis activities of the samples with suitable properties were studied. The results proved that the WO$_3$ properties can be affected by additive concentration and pH value of the solution. The creation of uniform nanorods (the length to diameter ratio of 9.4) was showed by FESEM analysis due to the addition of K$_2$SO$_4$. The smallest crystallite size (about 24.10 nm) was obtained for the sample synthesized at low concentration of potassium sulfate with the band gap of 2.64 eV (the ratio of Na$_2$WO$_4$2H$_2$O:K$_2$SO$_4$ 1:3). Furthermore, the 10 mg of synthesized nanorod displayed the meritorious degradation of methylene blue (10 ppm) under UV light and visible light with the degradation efficiency of 88% and 77% in 90 min, respectively.

1. Introduction

Photocatalysis oxidation method is the best way to solve the issue of environment pollution due to its high efficiency. This technology can turn organic contaminants into H$_2$O and CO$_2$ under light irradiation. The elimination of water pollution is one of the most significant applications of semiconductors. Besides, the photocatalysis activity depends on the different factors like crystalline structure, degree of crystallinity, surface area, shape, and size of particles. Hence, scientists have tried to synthesize different materials, including TiO$_2$, ZnO, WO$_3$, MoS$_2$/CdS, and TiO$_2$/SnO$_2$ [1-3]. Among them, tungsten oxide is counted as a more qualified catalyst due to its morphological diversity, various oxidation states, and narrow bandgap (2.7-3.5 eV) [4]. In addition, the structure and composition of WO$_3$ can affect its photocatalysis activity [5].

Many scientists have tried to achieve special morphologies of WO$_3$ through various techniques. Hence,

the hydrothermal method was widely employed in the fabrication of WO$_3$ nanostructures [6,7]. Also, different assisted agents such as organic materials, inorganic salts, and a combination of them have been utilized in the hydrothermal synthesis to obtain different morphologies e.g. flower-like, nanorods, nanoplates, and spherical [8,9]. Moreover, these additives were found to be effective intermediates to stabilize nanoparticles, control the size and stoichiometry, and to prevent nanoparticles agglomeration [10]. Wei and his co-workers applied organic surfactants like Malic acid (C$_4$H$_6$O$_5$) and Ammonium tartrate (C$_4$H$_{12}$N$_2$O$_6$) to form cauliflower-like hierarchical structure [11]. In another work, the nanorod and nanowire of tungsten oxides have been synthesized by applying Thiourea (NH$_2$CSNH$_2$) and Glycine acid (C$_2$H$_5$NO$_2$) as organic surfactants [12,13]. It has been shown that the organic acid had an effective coordination capacity with WO$_4$$^{2-}$ to prevent the aggregation. In addition, the organic

---

surfactant has a key role on the selective adsorption and growth rate of crystal facet of WO_3.

The utilization of oxalic acid, an organic surfactant, has known as an executable procedure for the synthesis of tungsten oxide nanostructures. Oxalic acid can coordinate via carboxylate functionalities to adsorb onto the surface of the nanoparticles and expose the carboxylic acid group. Then, the surface of nanoparticles become hydrophilic and stop their agglomeration. Furthermore, the surface of nanoparticle can be modified by the formation of various functional groups [14,15]. Li and co-workers have synthesized the different morphologies of tungsten oxide like cubic and spherical structures using oxalic acid as capping agent through hydrothermal method at 90°C for 3h. The value of pH is considered as an important parameter to the synthesis of WO_3 nanostructure in the hydrothermal method [16]. It is usually adjusted by adding hydrochloric acid with various molarity (concentration) [17,18].

On the other hands, inorganic additives have been also employed to fabricate WO_3 nanostructures. The hierarchical hollow nest-like and nanosheet structures of WO_3 were successfully synthesized by adding $Na_2C_2O_4$ [19] and $NaClO_4$ [20], respectively. Furthermore, sulfates were engaged as inorganic additives [21,22]. The interaction among the sulfates and the surface of crystals may have a significant role in controlling the morphology of the synthesized WO_3 nanostructures.

Wu and his co-workers reported that WO_3 nanorods were synthesized through adding oxalic acid and sodium sulfate to the tungstate solution. Their products degraded several organic dye molecules under xenon lamp irradiation [23]. Mehta [24] and Shen [25] have successfully obtained a self-assemble structure of tungsten oxide by adding oxalic acid and potassium sulfate simultaneously for the detection of ethanol vapor and NO_2 gas. They have used different kinds of acids (H_2SO_4 and HCl 3M, respectively) to adjust the pH value at 1 and achieved the various crystallite phases of hexagonal and orthorhombic, respectively. Also, Zeng and his coworkers obtained different morphologies of WO_3 from 0D to 3D using oxalic acid and potassium sulfate individually for the investigating of the gas sensing properties [26]. The pH adjustment stage can be effective on the properties of the nanomaterials in the presence of additives such as a surfactant. Patil and his co-workers have regulated the pH value at 1 before adding oxalic acid to synthesize Ti-doped WO_3 nanostructures [27]. Meanwhile, many scientists have controlled the pH value after pouring surfactants into the solution [13,16,24,28]. However, there is no comparison study on the stage of pH adjustment.

In this work, several amounts of oxalic acid have been selected as an organic surfactant to synthesize WO_3 nanostructure. In addition, the effect of pH adjustment time has been studied on the structural, morphological, and optical properties of hydrothermally synthesized WO_3. Also, potassium sulfate has been selected as an inorganic additive to fabricate WO_3 nanorods. Finally, the photocatalyst activity of the synthesized nanorod has been investigated.

2. Materials and methods

Sodium tungsten dihydrate, oxalic acid, and hydrochloric acid were purchased from Merk company, and applied without more purification as a starter, surfactant, and pH regulator, respectively. First, 3.3gr of $Na_2WO_4.2(H_2O)$ were added to 100 ml deionized water (DW) and the pH value was adjusted to 2 using few drops of HCl (2M). Then, oxalic acid was poured into the solution with different weight ratios. The ratios of oxalic acid to $Na_2WO_4.2(H_2O)$ were selected as 1:1, 0.5:1, 0.25:1, 0.125:1 and 0.0625:1 and the samples were correspondingly denoted as W_1, W_2, W_4, W_8, and W_{16}, respectively. In the second experiment, $Na_2WO_4.2(H_2O)$ (3.3 gr) and oxalic acid were dissolved in deionized water (DW) simultaneously with the ratios of 0.125:1 and 0.0625:1. Then, HCl was added to the above solution dropwise until the pH of the mixed solution reached 2. The samples were named $W_8(2)$ and $W_{16}(2)$, respectively. The solution was sealed in an100 ml autoclave and maintained at 180°C for 48h. Finally, the samples were washed with DW and ethanol several times, and were dried at 80°C for 12h.

For the third experiment, sodium tungstate dihydrate (3.3 gr) was used as a precursor, and potassium sulfate was added as a surfactant. HCl was employed to adjust the pH value at 2. The hydrothermal condition had been carried out same as the previous section. Different weight ratios of $Na_2WO_4 2H_2O:K_2SO_4$ (1:1, 1:2, 1:3, and 1:4) were selected. No powder was obtained for the first two concentrations of surfactant (1:1 and 1:2), and the other samples (1:3, and 1:4) were named as WP3 and WP4 respectively.

The structural, morphological, and optical characterizations of the products were performed by X-ray diffraction (XRD) (D8-Advance diffractometer employing CuKα radiation, fabricated by Brucker), field emission scanning electron microscopy (FESEM) (MIRA3, fabricated by Tescan), Raman (TakRam N1-541, Teksan Co) spectroscopy, and diffuse reflection spectroscopy (DRS) (Shimadzu, Uv-1800). In addition, N2 adsorption-desorption measurement was used to characterize the surface area and porosity analysis samples by using Brunauer-Emmett-Teller (BET) approach (Belsorb mini system). Also, the photocatalysis activities of 10 mg of WP3 sample were estimated for methylene blue (MB) solution with 10 ppm concentration under UV light at 380 nm and visible light and the MB degradation was obtained by measuring the absorbance of the MB solution at certain time intervals using spectrophotometry. Before irradiation, the MB solution in contact with photocatalyst was stirred for 120 min in the dark condition until reaching the adsorption-desorption equilibrium.

3. Results and discussion

3.1. Oxalic acid

3.1.1. The effect of surfactant concentration

3.1.1.1. XRD

The XRD patterns of W_1, W_2, W_4, W_8, and W_{16} samples are displayed in Figure 1. The results indicate that the phase transition from orthorhombic to hexagonal has occurred with the increment of oxalic acid concentration from 0.125:1 to 0.0625:1. In addition, the preferred growth direction changed upon phase transition. The orthorhombic and hexagonal phases were matched with

the ICDD-087-1203 (space group: Fmm2, lattice parameter: a=7.32Å, b=12.62 Å and c=7.81 Å) and JCPDS-033-1387 (space group: P6/mmm, lattice parameter: a=b=7.29 Å and c=3.89 Å) cards, respectively. The orthorhombic phase was related to the $WO_3 1.3H_2O$ structure. In the hydrothermal method, the dielectric constant of water diminishes with temperature enhancement. As a result, the electrostatic repulsion between W^{+6} ions becomes stronger and leads to the formation of the $WO_3 1.3H_2O$ structure [29].
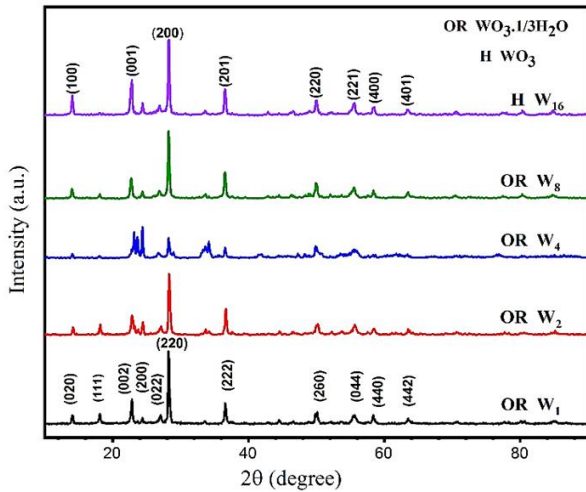

Fig. 1. The XRD patterns of WO_3 samples synthesized at different oxalic acid concentrations.

Table 1. Microstructural parameters of WO_3 nanoparticles synthesized at different oxalic acid concentrations.

Sample ID	Crystallite size (nm)	Microstrain	Dislocation density($1/nm^2$)
W_1	37.80	0.0057	6.999
W_2	46.51	0.0033	4.623
W_4	52.71	0.0065	3.599
W_8	37.67	0.0093	7.047
W_{16}	37.17	0.0054	7.238
$W_8(2)$	42.79	0.0047	5.461
$W_{16}(2)$	41.88	0.0049	5.701

Table 1 summarized the microstructural parameters of the samples including crystallite size, micro strain (ε), and dislocation density (δ) [30]. The average crystallite size of the W_1, W_2, W_4, W_8, and W_{16} samples are 37.80, 46.51, 52.71, 37.67, and 37.17 nm, respectively, as calculated using Williamson-Hall method [31]. According to Table 1, the crystallite size increased with increasing oxalic acid concentration from 1:1 to 0.25:1. However, it decreased with further increment of oxalic acid concentration. Since dislocation density depends on the crystallite size, a gradual change of dislocation density was observed in the same way as crystallite size variation. Also, minor changes were observed in another parameter such as microstrain.

3.1.1.2. Raman scattering spectroscopy

The Raman signals are sensitive to the crystal structure and its defects. Hence, the Raman spectra were recorded to study the structure of synthesized WO_3 nanostructures (Figure 2). Table 2 gives the peak position and related vibrational modes of the samples. The dominant vibrational mode of samples was labelled as symmetric stretching of W-O-W bridging oxygen bonds located at about 807 cm^{-1}. Another major peak was observed in the region of 927-943 cm^{-1} which belongs to a terminal W=O stretching mode of cluster boundaries. The W=O terminal corresponds to the W-O bond at the free surface of the internal grain that is created by water molecules [32]. Therefore, the reduction or elimination of the W=O bond can indicate the formation of the porous structure due to the removal of structural water. Also, Figure 3 depicts peaks in the range of 702-754 cm^{-1}, corresponding to O-W-O asymmetric stretching vibration mode [33]. Another Raman band found at the 603-673 cm^{-1} region can be ascribed to the asymmetric bending vibration of O-W-O. Obviously, there was a group of peaks with low intensities at about 243-329 cm^{-1} in the Raman spectra of the samples that are attributed to O-W-O symmetric bending vibration mode or O-W-O bond deformation [34,35].

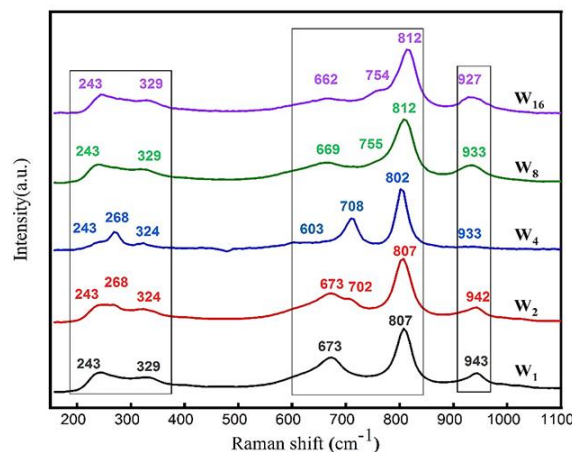**Fig. 2.** The Raman scattering spectra of WO3 synthesized with different concentrations of oxalic acid.

Table 2. The vibrational modes of synthesized samples with different oxalic acid concentration [17, 36].

Modes	Raman shift (cm^{-1})						
	W_1	W_2	W_4	W_8	W_{16}	$W_8(2)$	$W_{16}(2)$
W=O stretching	944-994	942-994	933	933	927	927	931
W-O-W symmetric stretching	807	807	801	812	812	812	812
O-W-O asymmetric stretching	-	702	708	714	754	752	714-760
W-O asymmetric bending	673	673	603	670	661	661	662
O-W-O symmetric bending	243-329	243-268-324	243-268-324	243-274-329	243-280-329	243-329	243-274-329

The chemical bond length of molecules and the residual stress can be the reason for partial shifts in the Raman peak positions. The higher bond length caused a movement toward shorter wavenumbers and vice versa [36]. Moreover, the Raman peak position shifts to higher/ lower wavenumbers due to the compressive/tensile stress increment [37].

In the following, the integrated intensity ratio is calculated for the W–O–W/ W=O bonds located at 807 and 943 cm^{-1}. The measured integrated intensity ratios were 5.39, 5.54, 49.37, 4.97, and 4.94 for W_1, W_2, W_4, W_8, and W_{16}, respectively. There is a correlation between integrated intensity ratio and the particle size [38]. Higher integrated intensity ratios relate to higher particle sizes.

3.1.1.3. Morphology

The morphology of the samples was investigated by FESEM images, as shown in Figure 3. The shapeless, agglomerated and non-uniform particles were observed for the sample W_1 (synthesized with high oxalic acid concentration) (Figure 3a). The nano-plates were formed in the W_2 sample that stick together and leads to a bigger particle size (Figure 3b). The nanoparticles were observed for W_4 sample with more homogeneity, although they were still stuck together (Figure 3c). By decreasing oxalic acid concentration, the limitations in the growth dimensions were removed, resulting in the formation of nanorods with diameters/lengths of about 129 nm/564 nm for the W_8 (Figure 3d) [16]. Figure 3e shows that the W_{16} sample tends to create nanorods with a longer length, greater diameter, reduced dissociability, and growth in batches. For this sample, the diameter and length of rods were calculated about 238 nm and 2322 nm, respectively. Generally, the reduction of oxalic acid has affected the formation and dimensions of nanoparticles. The less the surfactant amount, the longer the nanorod length.

It is concluded that although adding oxalic acid as a surfactant in the synthesis process results in directional growth, but the surfactant concentration is a critical parameter and high concentration is not favorable for growth of one dimensional nanorods.

The released oxalate ions ($C_2O_4^{-2}$) during the synthesis are responsible for shape and morphology control. The $C_2O_4^{-2}$ ions interact with the interlayer H_2O molecules in $WO_3.2H_2O$ nuclei, and destroy the formed hydrogen bonds. Then, the dehydration occurs in the $WO_3.2H_2O$ structure. The variation of oxalate ions concentration leads to change the formation of bonds and control of morphology, because the growth direction of different facets are influenced by the binding to particular facets [16, 39]. The high number of ions limits the particles growth. Also, it can cause separation of the interlayer water from structural water and then exit during washing and thermal treatment [40].

3.1.1.3. DRS analysis

The diffuse reflectance spectroscopy (DRS) measurements were surveyed to assay the light absorbance and the bandgap energy of the samples. From DRS results acquired in Figure 4, it can be concluded that all samples were highly reflective in the visible region. In addition, they significantly absorb light in the ultra-violet region. The minimum reflectance was observed at a wavelength around 300 nm for the W_8 sample. The absorption edges of the products are located around 434, 459, 473, 434, and 423 nm for W_1, W_2, W_4, W_8, and W_{16}, respectively. Upon decreasing oxalic acid concentration, firstly, the absorbance edge showed a red-shift (W_1 to W_4), then a blue-shift has been observed for W_8 and W_{16}.
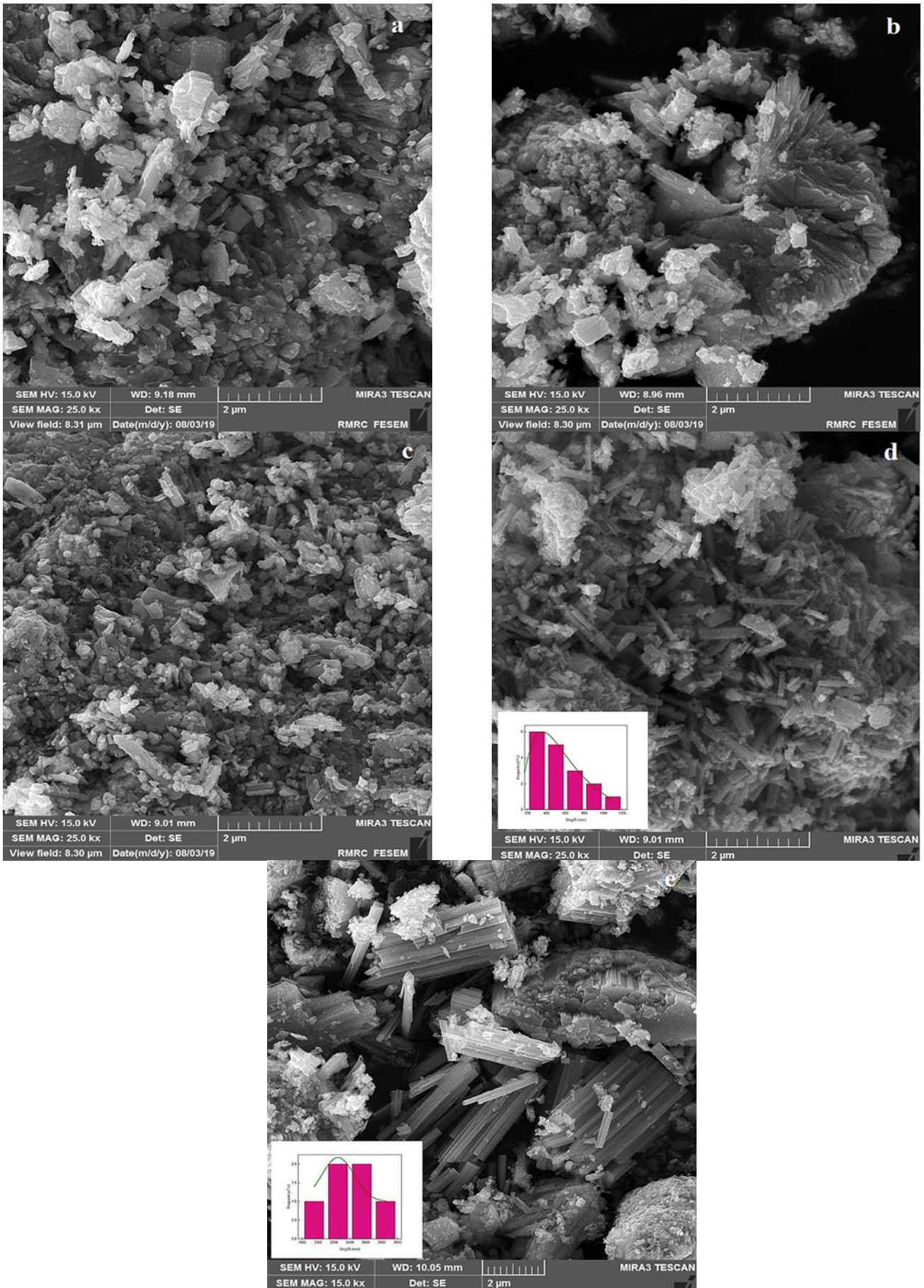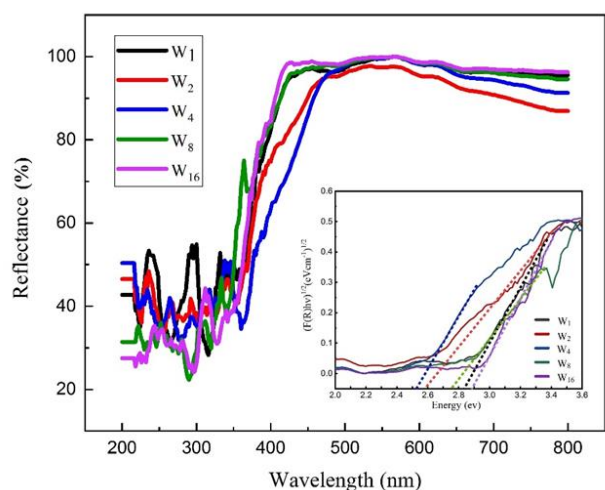
Fig. 3. The FESEM images of WO3 powders synthesized at different surfactant concentrations: a) W_1, b) W_2, c) W_4, d) W_8, and e) W_{16}.

Fig. 4. DRS spectra of WO3 nanostructures synthesized at different oxalic acid concentrations.

The energy bandgap (E_g) is one of the most important parameters in the semiconducting materials to predict their behavior under light illumination. In order to calculate the energy bandgap of the samples, Kubelka-Munk formula [41] and Tauc method [42] were employed, and the corresponding profile is given as an inset in Figure 5. As can be seen from Table 3, the lowest (2.55 eV) and highest (2.88 eV) bandgaps were related to W_4 and W_{16} samples, respectively. The results showed that the variations of absorption edge and bandgap were almost correlated with the variations of crystallite size, such that higher values of absorption edge and lower bandgaps occurred for the samples containing bigger crystallites. Furthermore, it seems that the crystal phase transformation of nanoparticles and surface plasmon resonance (SPR) effect of WO3 can affect the absorption edge of the samples [43], [44].

Table 3. The optical parameters of WO3 nanostructures synthesized at different surfactant concentrations.

Samples	Optical parameters			
	Bandgap (eV)	Absorption edge (nm)	E_{VB} (eV)	E_{CB} (eV)
W_1	2.83	434	3.50	0.67
W_2	2.58	459	3.38	0.80
W_4	2.55	473	3.36	0.82
W_8	2.77	434	3.47	0.71
W_{16}	2.88	423	3.53	0.65
$W_8(2)$	2.77	437	3.47	0.71
$W_{16}(2)$	2.66	476	3.42	0.76

Besides, the energy band potential of the samples was evaluated as a key parameter in the photochemical activity of WO3 nanostructure. The following relations (Equations

(1) and (2)) were used to obtain the valence band energy (E_{VB}) and the conduction band energy (E_{CB}):

$$E_{VB} = X - E_e + 0.5\, E_g \qquad (1)$$

$$E_{CB} = E_{VB} - E_g \qquad (2)$$

Where X is the absolute electronegativity of WO3 and E_e is the energy of free electron on the hydrogen scale that were found 6.59 eV and 4.5 eV, respectively [45]. Based on the achieved values mentioned in Table 3, the values of E_{VB} were more positive than hydroxyl group reduction potential (E°(OH/•OH) = 2.38 eV) for all the samples. It means that hydroxyl radicals can collaborate in the photochemical activity of the synthesized samples. In addition, the values of E_{CB} were more positive than oxygen reduction potential (E° (O_2/ •O_2^-) = -0.33). This implies that superoxide radicals cannot convert O_2 to •O_2^- under light emission in applications like photocatalyst.

3.1.2. The effect of pH adjustment stage

3.1.2.1. XRD

Fig. 5 represents the XRD patterns of the samples synthesized at two different oxalic acid concentrations (W_8 and W_{16}) with different pH adjustment stages. The identified diffraction peaks can be indexed to orthorhombic WO3.1.3H2O (ICDD-087-1203) and hexagonal WO3 (JCPDS 033-1387) for $W_8(2)$ and $W_{16}(2)$ samples, respectively. The phase transition was detected from orthorhombic to hexagonal for the W_8 sample upon changing pH adjustment stage, but there was no phase difference between W_{16} and $W_{16}(2)$ samples. The crystallite size was obtained 42.79 nm and 41.88 nm for $W_8(2)$ and $W_{16}(2)$, respectively. Therefore, the crystallite size was slightly decreased with the surfactant decrement in this pH adjustment method, too. However, an enhancement was observed in the crystallite size of $W_8(2)$ and $W_{16}(2)$ compared to the W_8 and W_{16} samples. This can be attributed to the pH adjustment stage in the synthesis process. The final pH of the solution was different for the two synthesis methods because the used surfactant (oxalic acid) is acidic in nature. The higher pH (in the second method) leads to the formation of larger crystals due to the lower number of capping agent molecules in the solution [46]. Also, other microstructural parameters like microstrain, dislocation density, and stacking fault were changed according to the crystallite size variation as denoted in Table 1.
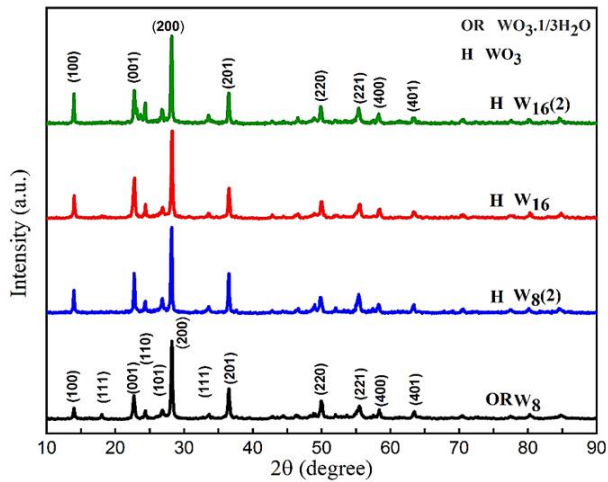
Fig. 5. The XRD patterns of W8 and W16 samples with different pH adjustment stage.

3.1.2.2. Raman scattering spectroscopy

The Raman scattering spectra of $W_8(2)$ and $W_{16}(2)$ samples are shown in Figure 6. The corresponding bonds were summarized in Table 2. A slight shift was happened in the Raman peaks positions which its reason was explained earlier in section 3.1.2. The integrated intensity of W-O-W/W=O peaks was obtained 4.96 and 6.99 for the $W_8(2)$ and $W_{16}(2)$, respectively. An increment in the values of integrated intensity ratio of W−O−W/W=O was found with decreasing oxalic acid concentration. Furthermore, the integrated intensity ratio was almost similar for W_8 and $W_8(2)$ samples, but it was greater in the case of the $W_{16}(2)$ sample compared with W_{16}. This suggests that the crystallinity of $W_{16}(2)$ was enhanced compared with W_{16}.
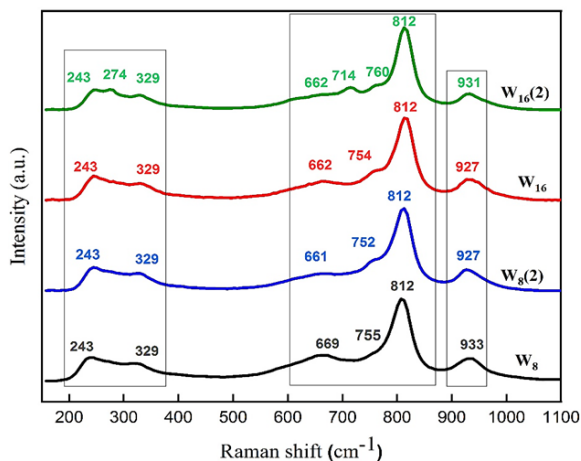

Fig. 6. Raman scattering spectra of W8 and W16 samples synthesized under different pH adjustment stage.

3.1.2.3. Morphology

As shown in Figure 7, the FESEM images of the samples, nanorods were formed with more uniformity toward W_8 and W_{16}. It was due to the low concentration of surfactant that reduced applied restrictions on the particles. The diameter and length of the nanorods were estimated about 373 and 1433 nm for the $W_8(2)$ and around 354 and 1779 nm for the $W_{16}(2)$. Decreasing the amount of surfactant has

increased the length of the nanorods and has prevented them from accumulating [47]. Although the length of nanorods decreased for the $W_{16}(2)$ sample compared to the W_{16}, the aspect ratio was increased for both samples in the second method of pH adjustment, which leads to an increment in the surface area of the samples.
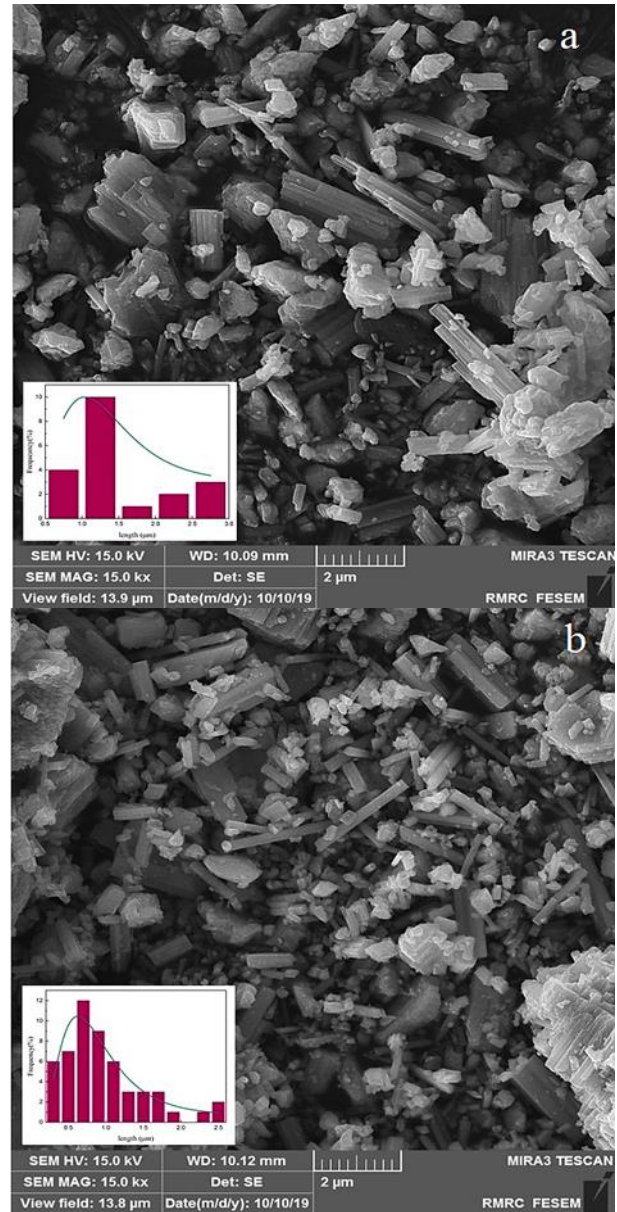

Fig. 7. The FESEM images of a) $W_8(2)$ and b) $W_{16}(2)$ specimens.

In conclusion, as the existence of cationic ions like Na^+ play key roles in the formation of various WO_3 nanostructures, the pH adjustment process can affect the amount of NaCl cussed by the reaction between HCl and Na_2WO_4 in the solution [48]. More Na^+ ions lead to further control of WO_3 nucleus. When Oxalic acid is added before pH adjustment, the initial pH of solution decreases, so more HCl is needed to adjust the pH value at 2 which results in formation of more NaCl to control the morphology and hence the different properties of WO_3 nanostructures.

3.1.2.3. DRS analysis

According to DRS plot (Figure 8), there were no remarkable changes in the reflectance of the samples in the visible region. The minimum reflectance corresponded to the $W_8(2)$ sample. It was also observed that the minimum reflection for the sample synthesized by the second method of pH adjustment had a lower intensity, resulting in more absorption in the ultraviolet region. The absorption edges were estimated around 433 nm and 476 nm for $W_8(2)$ and $W_{16}(2)$, respectively. The absorption edge was enhanced in the second method as well as with the decrement of surfactant concentration. Despite of decreasing bandgap energy for $W_{16}(2)$ compared to W_{16}, the same values were achieved for W_8 and $W_8(2)$ samples (Table 3). This result was also inferred from the appearance of reflection spectra. The valence band energy (E_{VB}) and the conduction band energy (E_{CB}) were evaluated, and the variation of the values was found to depend on the bandgap energy variations. Generally, because of increasing the pH value of the solution in both cases (i.e., surfactant concentration decrement and second method of the pH adjustment), the variation of optical properties can be attributed to the pH effect [18].
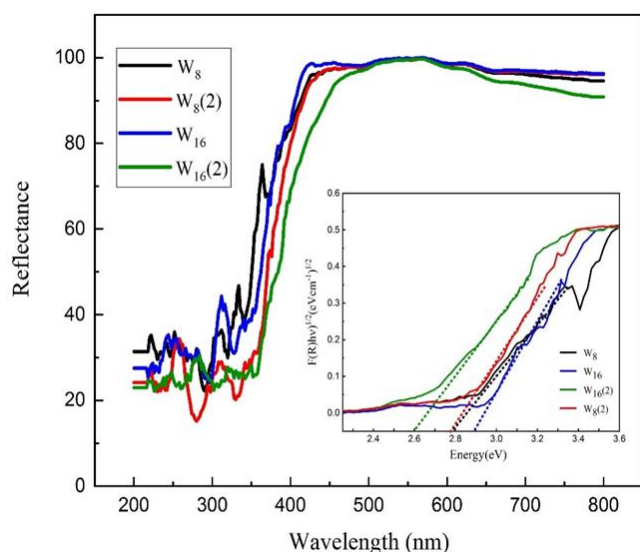

Fig. 8. The DRS spectra of WO₃ nanostructures synthesized with different pH adjustment stage.

Generally, the utilization of oxalic acid can affect the properties of WO₃ nanostructures via the variation of synthesis conditions. For example, the nanosheet structure of WO₃ has been synthesized through the microwave method at 200 ºC for 30 min with the band gap of 2.53 eV [49]. Also, co-precipitation method and oxalic acid have been employed to the fabrication of the WO₃ nanoparticles using other surfactants like N- trimethylammonium bromide (CTAB) (crystallites size of 9.58 nm and band gap 2.86 eV) and Sodium dodecyl sulfate (SDS) (crystallites size of 11.2 nm and band gap 2.92 eV) in addition to oxalic acid to control of WO₃ properties [50].

3.2. Potassium sulfate

3.2.1. XRD

As can be seen in Figure 9, the XRD patterns of synthesized WO₃ samples using different concentrations of K_2SO_4 as a surfactant, the diffraction peaks of the samples are consistent with the hexagonal WO₃ (JCPDS No.075-2178). Compared to first experiment, the crystalline phase of the sample has not changed, but the intensity of the peaks has greatly decreased because of the addition of surfactant. This indicates the decrease in order and the increase in the formation of defects. Moreover, the crystallite size of the samples was calculated using the Williamson-Hall method [31] (Table 4). The results show that the addition of K_2SO_4 leads to a decrease in crystallite size. When K_2SO_4 is dissolved in an aqueous solution containing Na_2WO_4, K^+ ions with a larger radius than Na^+ ions are released. These ions are surrounded by water molecules and form hydrated K^+ with a smaller radius than hydrated Na^+ ions. The hydrated K^+ and Na^+ ions surround the nucleus of WO₃ and then restrict the growth of particles [51]. However, surfactant enrichment (1:4 weight ratio) led to an increase in crystallite size, microstrain, and dislocation density.
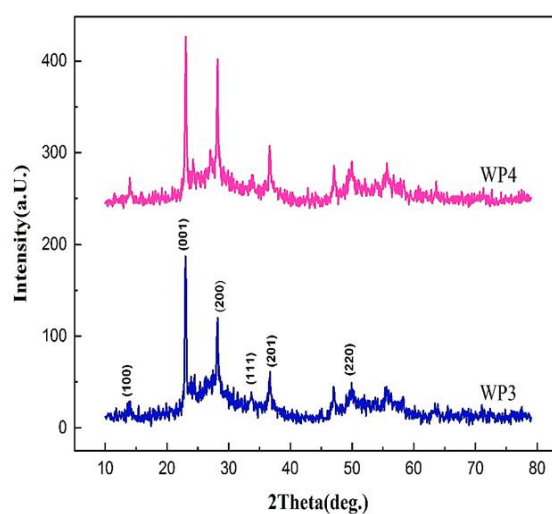
Fig. 9. XRD patterns of WO₃ nanostructures synthesized at different concentrations of K_2SO_4.

Table 4. The structural parameters of WO₃ nanostructures synthesized at different concentrations of K_2SO_4.

Sample	Crystallite size (nm)	Microstrain	Dislocation density (1/nm²)
WP3	24.10	0.0032	1.72
WP4	41.5	0.0055	5.81

3.2.2. Raman scattering spectroscopy

Fig. 10 illustrates the Raman spectra of WP3 and WP4 samples. There are three main regions in the Raman spectra of WO₃, divided into 200- 400, 600-800, and 900-

1000 nm, which belong to the bending modes of W-O-W, the stretching vibrations of W-O, and the terminal oxygen atoms, respectively. The presence of the highest peak around 800 cm^{-1} confirmed the formation of crystalline WO_3 [52]. The variation in molecular length can change the position of the peaks, i.e., the longer (shorter) bond length causes a shift to a lower (higher) wavenumber [36].

The intensity of the Raman peaks does not change considerably with increasing the K_2SO_4 concentration, indicating almost similar crystalline quality of WP3 and WP4 samples. The obtained result is in agreement with the XRD.
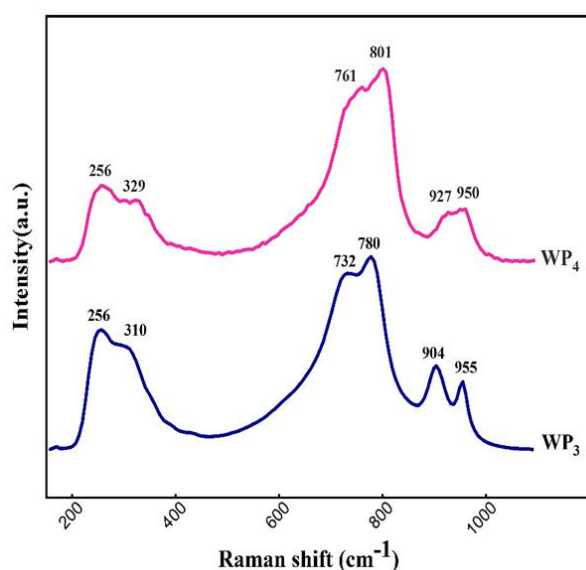

Fig. 10. Raman spectroscopy of WO_3 nanostructures synthesized at different concentration of K_2SO_4.

3.2.3. FESEM

The FESEM images of the synthesized samples are shown in Figure 11. The nanorods were formed uniformly. The nanorods have a longer length with a higher aspect ratio in the WP3 sample than WP3 sample. Although the uniform nanorods were observed in WP4, the length of nanorods decreased and the diameter increased with the increase in the concentration of surfactant. The ratio of length to diameter was 9.4 and 7 for WP3 and WP4 samples, respectively. As described in section 3.1, potassium ions play a key role in the formation of nanorods. However, increasing the number of K$^+$ ions in the solution results in excessive potassium ions surrounding each nucleus and limiting nanorods growth. By comparing these results with those obtained for samples prepared using oxalic acid, it is concluded that K_2SO_4 is a much more suitable additive for controlling the morphology and formation of more uniform and dispersed nanorods with higher aspect ratios.

A possible growth mechanism for forming the uniform WO_3 nanorod is explained according to the equation in Figure 12 [53]. The Na$^+$ and K$^+$ ions form after the interaction between precursors in the solution mediate. These ions act as directing agents to control the

morphology of the initial nuclei of WO_3 formed at the beginning of the hydrothermal reaction. Besides, the (200) plane of WO_3 provides more adsorbed opportunity of cations at the initial step as compared with the (001) plane because of the energy difference between (001) and (200) faces. Hence, the growth of (200) plane will be restrict by ions adsorption. As a result, WO_3 nanoparticles continuously grow along [001] direction to form uniform nanorods with a high aspect ratio.
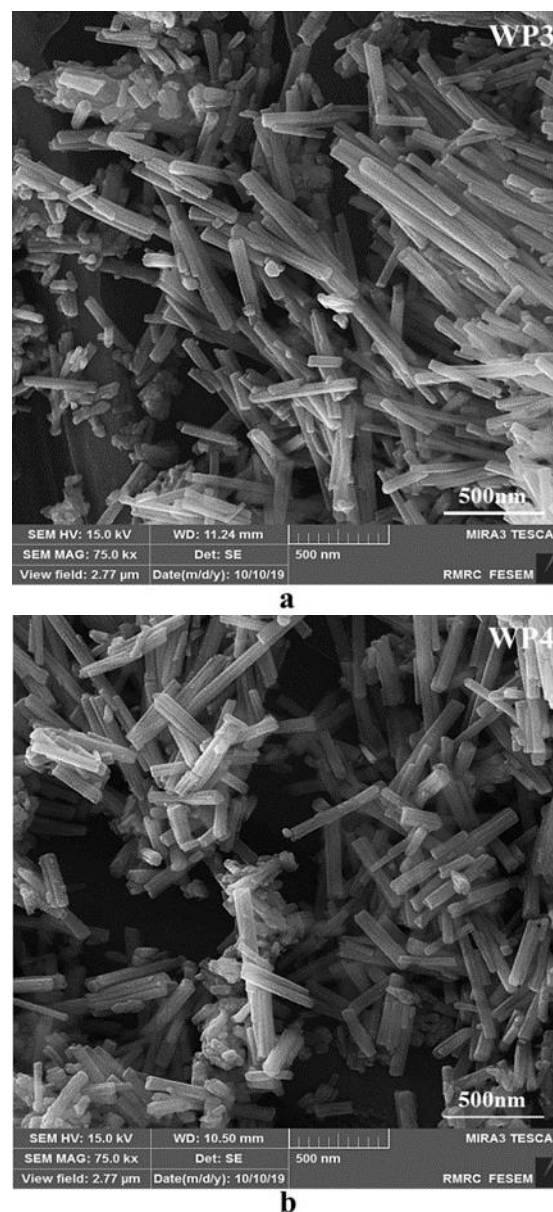

Fig. 11. The FESEM image of the WO_3 nanostructures synthesized at the different concentrations of K_2SO_4.
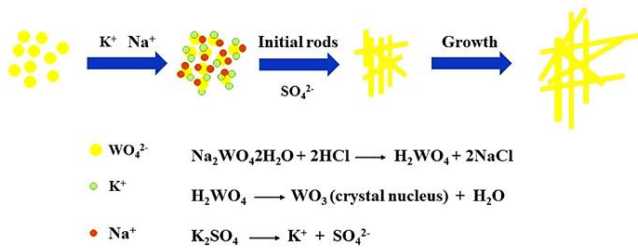
Fig. 12. The schematic of the growth mechanism of WO₃ nanorods.

3.2.4. DRS

DRS technique was applied to study the optical properties of the synthesized samples (WP3 and WP4). As shown in Figure 13, the samples have weak absorbance in the visible region due to the defect states and surface trap states [54]. The absorption edges are located at 455 and 453 nm for WP3 and WP4 samples, respectively. The maximum absorption is observed in the ultraviolet region (around 330 nm) for both samples. It is also noticed that, in the case of using K_2SO_4 as a surfactant, the reflectance values of the samples in the UV region are significantly lower than those of the samples synthesized using oxalic acid observed in previous sections. This can be useful for the optical applications such as photocatalytic process.

The bandgap energy was computed using the Kubelka-Munk function and the Tauc method. The values of the calculated bandgaps are reported in Table 4. The WP3 sample showed lower bandgap (2.64 eV) than WP4 (2.76 eV) one. The variation of surfactant concentration leads to minor changes in the structural properties and bending energy. As a result, the bandgap energy is modified because of a direct dependency on these parameters.
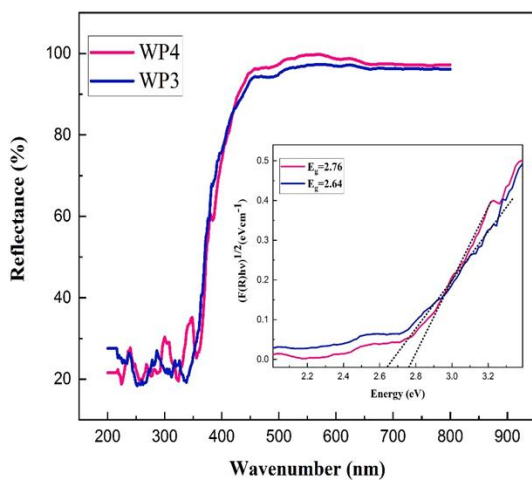

Fig. 13. DRS spectra of WO₃ nanostructures synthesized at the different concentrations of K_2SO_4.

Table 4. The optical parameters of WO₃ nanostructures synthesized at different K_2SO_4 concentrations.

Sample	Bandgap (eV)	Absorption edge (nm)	E_{VB} (eV)	E_{CB} (eV)
WP3	2.64	455	3.41	0.77
WP4	2.76	453	3.47	0.71

4. Photocatalyst activity

The WP3 sample was selected to study photocatalysis activity because of its smaller crystallite size, more uniform morphology, and a lower bandgap. Since the specific surface area can be an effective parameter for photocatalysis activity of nanomaterials, the nitrogen adsorption-desorption isotherm and pore size distribution of the products are presented in Figure 14. The curve of the samples is classified as Type-V isotherm and contained an H3 hysteresis loop at a relative pressure (P/P0) around 0.2-0.9 for WP3 and 0.7-0.9 for WP4. Both samples are characterized as mesoporous structures because the average pore sizes are about 32.10 and 32.44 nm for WP3 and WP4, respectively. The specific surface area decreased from 52.29 m²/g (WP3) to 27.08 m²/g (WP4) with the increase of surfactant concentration.
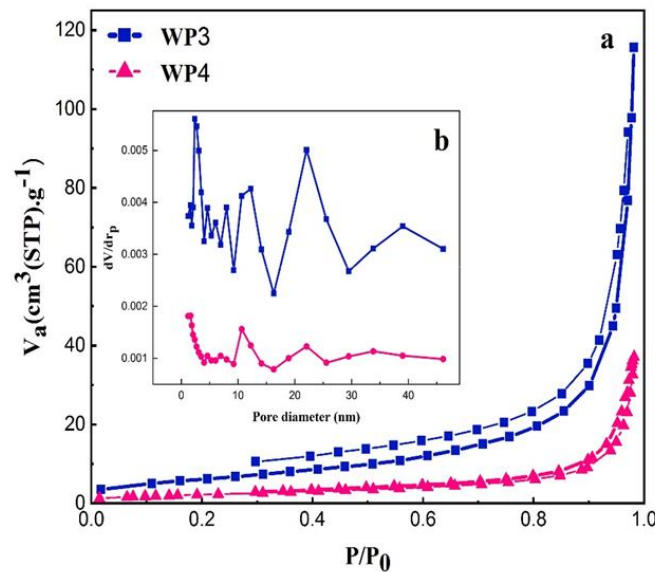

Fig. 14. (a) The N₂ adsorption-desorption isotherm and (b) the corresponding pore size distribution of WO₃ nanostructures synthesized at the different concentrations of K_2SO_4.

Methylene blue (MB) was used as a pollutant, and the photocatalytic process was done under ultraviolet and visible light irradiations. Since the decrease in the intensity of the MB adsorption peak indicates its degradation, it can be concluded that more degradation has taken place under ultraviolet radiation (Figure.15a-c). The maximum degradation efficiency was obtained 88% and 77% in the 90 min irradiation of UV light and visible light, respectively. This can be related to the more absorbance of WP3 in the ultraviolet region explained in section 3.2.4.

According to Langmuir- Hinshelwood theory [55], the reaction rate was calculated about 0.0089 min⁻¹ and 0.0046 min⁻¹ under UV light and visible light irradiation,

respectively [56] and shown in Figure 16. The higher reaction rate under ultraviolet irradiation is due to the more generation of electron-hole pairs in the reaction [57].

After MB adsorption and light irradiation on the catalysis surface, the absorbed photons excite electrons and transfer them to the conduction band. Therefore, a hole in the valance band and reactive electron-hole pairs will be created. These holes react with water and hydroxide ions and create hydroxide radicals. On the other hand, the adsorbed oxygen on the surface reacts with excited electrons and produce active peroxide radicals [55]. The reaction products will participate in the decomposition of dye and finally turn to oxidized mineral acids, water and carbon dioxide [58].

In addition to the above mechanism, physical surface adsorption due to Van der Waals forces is an effective process in photocatalysis [59]. In this case, the dye molecules are excited under light irradiation and then, the released electrons transfer to the conduction band. These electrons move to the surface of the catalyst, react with the oxygen, and produce peroxide radicals, hydrogen peroxide, and hydroxyl radicals.

The obtained photocatalytic MB degradation of the synthesized tungsten oxide samples can be compared with the previous studies in the literature. For example, WO_3 nanorods have been prepared by a hydrothermal method using Na_2WO_4 and HCl as the raw materials and K_2SO_4 as a surfactant with the MB degradation efficiency from 48% to 97%. The hydrothermal temperature and hydrothermal time were considered as variable parameters from 120 ºC to 200 °C and from 12 h to 32 h, respectively [60]. Furthermore, Gadolinium doped WO_3 nanorods were synthesized via hydrothermal method and different surfactant like oxalic acid and sodium sulfate. The increasing of Gd concentration decreased band gap energy from 2.8 eV to 2.64 eV, and the degradation efficiency of organic Rhodamine B dye solution changed from 75% for pure WO_3 to 94 % for 5% Gd-WO_3 [61]. Therefore, the prepared samples in our work show a notable photocatalytic performance comparing to the reported results at the similar synthesis conditions and could be regarded as the aim of future studies on wastewater treatment application.
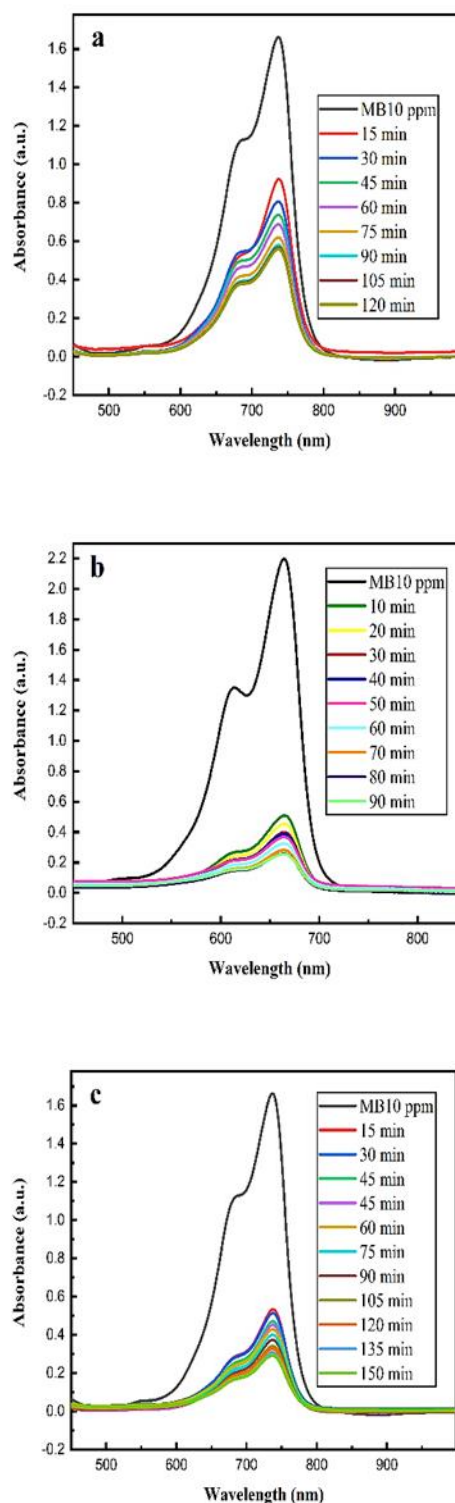
Fig. 15. (a) The UV- vis spectra of MB in dark and photocatalysis degradation of MB of WP3 (b) in ultraviolet light and (c) in visible light.
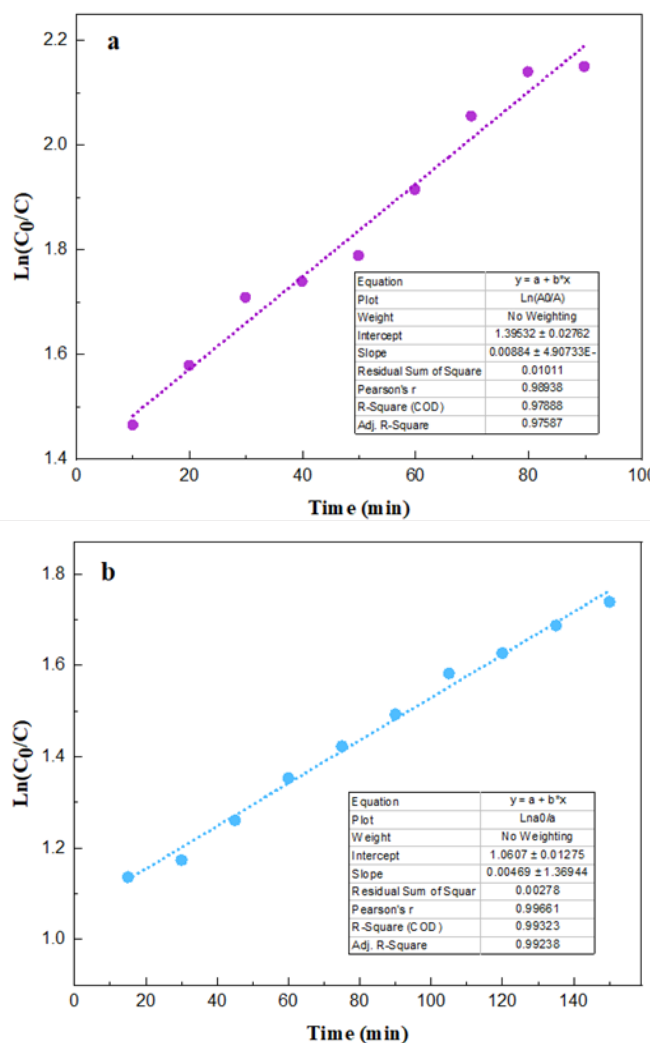
Fig. 16. The logarithmic diagram of concentration changes of MB in the presence of WP3 under (a) UV light and (b) visible light irradiation.

4. Conclusion

In this work, the surfactant-assisted hydrothermal synthesis of WO$_3$ nanostructures has been demonstrated and the effects of surfactant (oxalic acid and potassium sulfate) concentration and the pH adjustment method were studied on the structural and optical properties of the nanostructures. The results proved that the variation of the additives amount completely affected the structural, morphological, and optical properties of tungsten oxide., Raman spectra proved the formation of WO$_3$ nanostructures because of the existence of the correlated bonds in the spectra. The FESEM images showed that created nanorods have been evolved by decreasing the surfactant concentration for both organic and inorganic surfactants. In addition, the study of the pH adjustment method revealed that it had a minor effect on the size and optical properties of the nanoparticles, but the morphology became more uniform when the pH value was adjusted after the addition of surfactant. It can be related to the pH effect on the nucleation and growth process of nanoparticles. Finally, the photocatalysis activity was studied under UV and visible light irradiation for the sample synthesized using lower concentration of K$_2$SO$_4$ (WP3) because of its more uniform morphology with

higher aspect ratio (9.4), lower crystallite size (24.10), and higher specific surface area (52.29 m^2/g). Since the DRS spectra have shown higher absorption in the UV region for WP3, more decomposition of MB was observed during UV light irradiation (88%) than the visible light irradiation (77%). However, the decomposition of MB was reached 81% after 150 min under visible light irradiation. This can be explained by the rate of reaction under UV (0.0088 min^{-1}) and visible (0.0046 min^{-1}) irradiations.

References

[1]   M. Bellardita, A. Di, B. Megna, L. Palmisano, " Environmental Absolute crystallinity and photocatalytic activity of brookite TiO2 samples." Applied Catalysis B: Environmental 201 (2017) 150–158.

[2]   A. Mohammad, M.E. Khan, M.H. Cho, T. Yoon, "Fabrication of binary SnO2/TiO2 nanocomposites under a sonication-assisted approach: Tuning of band-gap and water depollution applications under visible light irradiation." Ceramica International 47 (2021) 15073–15081.

[3]   S.A. Darsara, M. Seifi, M.B. Askari, "One-step hydrothermal synthesis of MoS2/ CdS nanocomposite and study of structural, photocatalytic, and optical properties of this nanocomposite." Optik 169 (2018) 249–256.

[4]   Y.Fan, X.Xi, Y.Liu, Z.Nie, Q.Zhang, L.Zhao, "Growth mechanism of immobilized WO3 nanostructures in different solvents and their visible-light photocatalytic performance." Journal of Physics and Chemistry of Solids 140 (2020) 109380.

[5]   I.M. Szilágyi, B. Fórizs, O. Rosseler, A. Szegedi, P. Németh, "WO3 photocatalysts: Influence of structure and composition." Journal of Catalysis 294 (2012) 119–127.

[6]   Z. Jin, P. Hu, W. Xu, J. Zhou, W. Guo, Y. Chen, "Hydrothermal synthesis and gas sensing properties of hybrid WO3 nano-materials using octadecylamine." Journal of Alloys and Compounds 785 (2019) 1047–1055.

[7]   Z. Wei, Q. Zhou, J. Wang, W. Zeng, "Hydrothermal synthesis of hierarchical WO3/ NiO porous microsphere with enhanced gas sensing performances." Materials Letters 264 (2020) 127383.

[8]   Z.Cai, H.Li, J.Ding, X.Guo, "Chemical Hierarchical flowerlike WO3 nanostructures assembled by porous nanoflakes for enhanced NO gas sensing." Sensors Actuators B: Chemistry 246 (2017) 225–234.

[9]   H. Ahmadian, F.S. Tehrani, M. Aliannezhadi, "Hydrothermal synthesis and characterization of WO3 nanostructures: effects of capping agent and pH." Materials Research Express 6 (2019) 105024.

[10]   G. Bisht, S. Rayamajhi, "ZnO Nanoparticles: A Promising Anticancer Agent." Nanobiomedicine 3 (2016) 1-9.

[11]   S. Wei, J. Zhao, B. Hu, K. Wu, W. Du, M. Zhou, "Hydrothermal synthesis and gas sensing properties of hexagonal and orthorhombic WO3 nanostructures." Ceramica International 43 (2017) 2579–2585.

[12]   Q. Hu, J. He, J. Chang, J. Gao, J. Huang, L. Feng, "Needle-Shaped WO3 Nanorods for Triethylamine Gas Sensing." ACS Applied Nano Materials 3 (2020) 9046–9054.

[13]   S. Lin, Y. Guo, X. Li, Y. Liu, "Glycine acid-assisted green

hydrothermal synthesis and controlled growth of WO3 nanowires." Materials Letters 152 (2015) 102–104.

[14]   A. Sharma, D. Baral, H.B. Bohidar, P.R. Solanki, "Oxalic acid capped iron oxide nanorods as a sensing platform." Chemico-Biological Interactions 238 (2015) 129-137.

[15]   M. Ahmadi, J.F. Maxime, R.Y. Guinel, "Synthesis of Tungsten Oxide Nanoparticles using a Hydrothermal Method at Ambient Pressure." Journal of Materials Research 29 (2014) 1424–1430.

[16]   L. Li, J. Zhao, Y. Wang, Y. Li, D. Ma, Y. Zhao, S. Hou, "Oxalic acid mediated synthesis of WO3.H2O nanoplates and self-assembled nanoflowers under mild conditions." Journal of Solid State Chemistry 184 (2011) 1661–1665.

[17]   F. Mehmood, J. Iqbal, T. Jan, W. Ahmed, Q. Mansoor, S.Z. Ilyas, M. Ismail, I. Ahmad, "Effect of Sn doping on the structural, optical, electrical and anticancer properties of WO3 nanoplates." Ceramica International 42 (2016) 14334–14341.

[18]   M. Jamali, F.S. Tehrani, "Thermally stable WO3 nanostructure synthesized by hydrothermal method without using surfactant." Materials Science and Engineering: B 270 (2021) 115221.

[19]   R. Rong, L. Wang, "Synthesis of hierarchical hollow nest-like WO3 micro/nanostructures with enhanced visible light-driven photocatalytic activity." Journal of Alloys and Compounds 850 (2021) 156742.

[20]   T. Nagyné-Kovács, I.E. Lukács, A. Szabó, K. Hernadi, T. Igricz, K. László, "Effect of pH in the hydrothermal preparation of monoclinic tungsten oxide." Journal of Solid State Chemistry 281 (2020) 1–7.

[21]   W. Xu, C. Qiu, J. Zhou, Y. Chen, "Regulation of specific surface area of 3D flower-like WO3 hierarchical structures for gas sensing application." Ceramica International 46 (2020) 11372–11378.

[22]   T. Govindaraj, C. Mahendran, V.S. Manikandan, R. Suresh, R. "One-pot synthesis of tungsten oxide nanostructured for enhanced photocatalytic organic dye degradation." Journal of Materials Science: Materials in Electronics 31 (2020) 17535–17549.

[23]   S. Yao, F. Qu, G. Wang, X. Wu, "Facile hydrothermal synthesis of WO3 nanorods for photocatalysts and supercapacitors." Journal of Alloys and Compounds 724 (2017) 695–702.

[24]   S.S. Mehta, M.S. Tamboli, I.S. Mulla, S.S. Suryavanshi, "Facile hydrothermal synthesis of nanobricks assembled WO3 microflowers and their ethanol sensing properties." Materials Letters 217 (2017) 80–84.

[25]   Y. Shen, X. Chen, W. Wang, Y. Gong, S. Chen, J. Liu, D. Wei, D. Meng, X.S an, "Complexing surfactants-mediated hydrothermal synthesis of WO3 microspheres for gas sensing applications." Materials Letters 163 (2016) 150–153.

[26]   Y. Yu, W. Zeng, M. Xu, X. Peng, "Hydrothermal synthesis of WO3·H2O with different nanostructures from 0D to 3D and their gas sensing properties." Physica E: Low-dimensional Systems and Nanostructures 79 (2016) 127–132.

[27]   V.B. Patil, N.L. Tarwal, S.H. Mujawar, L.S. Mulla, P.S. Walke, S.S. Suryavanshi, "Enhanced NO2 response of hydrothermally grown Ti doped WO3 nanostructures."

Journal of Materials Science: Materials in Electronics 28 (2017) 1612–1619.

[28]   S. Wei, J. Zhao, B. Hu, K. Wu, W. Du, M. Zhou, "Hydrothermal synthesis and gas sensing properties of hexagonal and orthorhombic WO3 nanostructures." Ceramica International 43 (2017) 2579-2585.

[29]   B. Gerand, G. Nowogrocki, "A New Tungsten Trioxide Hydrate, WO3.1/3H2O: Preparation, and Crystallographic Study." Journal of Solid State Chemistry 38 (1981) 312–320.

[30]   L. Renuka, K.S. Anantharaju, S.C. Sharma, H. Nagabhushana, Y.S. Vidya, H.P. Nagaswarupa, S.C. Prashantha, "A comparative study on the structural, optical, electrochemical and photocatalytic properties of ZrO2 nanooxide synthesized by different routes." Journal of Alloys and Compounds 695 (2017) 382–395.

[31]   E. Taju, F.B. Dejene, R.E. Kroon, "Synthesis, characterization and influence of pH on indium doped zinc oxide nanostructures." Ceramica International 45 (2019) 24269–24278.

[32]   M.F. Daniel, B. Desbat, J.C. Lassegues, B. Gerand, M. Figlarz, "Infrared and Raman study of WO3 tungsten trioxides and WO3.xH2O tungsten trioxide tydrates. Journal of Solid State Chemistry 67 (1987) 235–247.

[33]   R.F. Garcia-Sanchez, T. Ahmido, D. Casimir, S. Baliga, P. Misra, "Thermal effects associated with the raman spectroscopy of WO3 gas-sensor materials." The Journal of Physical Chemistry A 117 (2013) 13825–13831.

[34]   B. Behera, S. Chandra, "Synthesis of WO3 nanorods by thermal oxidation technique for NO2 gas sensing application." Materials Science in Semiconductor Processing 86 (2018) 79–84.

[35]   F. Zheng, M. Zhang, M. Guo, "Controllable preparation of WO3 nanorod arrays by hydrothermal method." Thin Solid Films 534 (2013) 45–53.

[36]   M. Jamali, F. Shariatmadar Tehrani, "Effect of synthesis route on the structural and morphological properties of WO3 nanostructures." Materials Science in Semiconductor Processing 107 (2020) 1–6.

[37]   M. Dong, Q. Deng, Y. Zhang, T. Hang, M. Li, "Study on the relationship between Cu protrusion behavior and stresses evolution in the through-silicon via characterized by in-situ µ-Raman spectroscopy." Microelectronics Reliability115 (2020) 113949.

[38]   C. Vargas-Consuelos, K. Seo, M. Camacho-López, O.A. Graeve, "Correlation between particle size and raman vibrations in WO3 powders." The Journal of Physical Chemistry C 118 (2014) 9531–9537.

[39]   D. Meng, G. Wang, X. San, Y. Song, Y. Shen, "Synthesis of WO3 flower-like hierarchical architectures and their sensing properties." Journal of Alloys and Compounds 649 (2015) 731–738.

[40]   R. Huirache-Acuña, F. Paraguay-Delgado, M.A. Albiter, J. Lara-Romero, R. Martínez-Sánchez, "Synthesis and characterization of WO3 nanostructures prepared by an aged-hydrothermal method." Materials Characterization 60 (2009) 932–937.

[41]   P.Norouzzadeh, K.Mabhouti, M.Golzan, R. Naderali, "Investigation of structural , morphological and optical characteristics of Mn substituted Al-doped ZnO NPs : A Urbach energy and Kramers-Kronig study."

International Journal for Light and Electron Optics204 (2020) 164227.

[42] N.A. Al-balushi, A.T. Kuvarega, S. Karthikeyan, R. Selvaraj, "Thermal and hydrothermal synthesis of WO3 nanostructure and its optical and photocatalytic properties for the degradation of Cephalexin and Nizatidine in aqueous solution." Materials Science and Engineering: B 264 (2021) 114991.

[43] M. Parthibavarman, M. Karthik, S. Prabhakaran, "Facile and one step synthesis of WO3 nanorods and nanosheets as an efficient photocatalyst and humidity sensing material." Vacum 155 (2018) 224-232.

[44] V.A. Online, J. Li, J. Zhu, X. Liu, "Synthesis, characterization and enhanced gas sensing performance of WO3 nanotube bundles." New Journal of Chemistry 12 (2013) 4241–4249.

[45] L. Maria, A. Rougier, A. Duta, "Comparative investigation of the Ti and Mo additives influence on the opto-electronic properties of the spray deposited WO3 thin films." Journal of Alloys and Compounds 630 (2015) 133–145.

[46] M. Tsega, F.B. Dejene, "Influence of acidic pH on the formulation of TiO2 nanocrystalline powders with enhanced photoluminescence property." Heliyon 3 (2017) 246.

[47] M. Xu, W. Zeng, F. Yang, L. Chen, "Controllability of assemblage from WO3.H2O nanoplates to nanoflowers with the assistance of oxalic acid." Journal of Materials Science: Materials in Electronics 26 (2015) 6676–6682

[48] P. Shandilya, S. Sambyal, R. Sharma, P. Mandyal, B. Fang, "Properties, optimized morphologies, and advanced strategies for photocatalytic applications of WO3 based photocatalysts." Journal of Hazardous Materials 428 (2022) 128218..

[49] H. Liu, L. Duan, K. Xia, Y. Chen, Y. Li, S. Deng, "Microwave Synthesized 2D WO 3 Nanosheets for VOCs Gas Sensors." Nanomaterials 12 (2022) 1–11.

[50] T. Subramani, G. Thimmarayan, B. Balraj, N. Chandrasekar, "Surfactants assisted synthesis of WO3 nanoparticles with improved photocatalytic and antibacterial activity: A strong impact of morphology." Inorganic Chemistry Communications142 (2022) 109709.

[51] Q. Huang, W. Wei, J. Sun, S. Mao, "Hexagonal K2W4O13 Nanowires for the Adsorption of Methylene." ACS Applied Nano Materials 2 (2019) 3802–3812.

[52] A. Chaudhary, D. Pathak, M. Tanwar, R. Dash, B. Joshi, T. Keerthivasan, "Hydrothermally grown nano-WO3 electrochromic film: structural and Raman spectroscopic study." Advances in Materials and Processing Technologies (2020) 1–7.

[53] Z. Wei, Q. Zhou, Z. Lu, L. Xu, Y. Gui, C. Tang, "Morphology controllable synthesis of hierarchical WO3 nanostructures and C2H2 sensing properties." Physica E: Low-dimensional Systems and Nanostructures 109 (2019) 253–260.

[54] L. Kumari, G.H. Du, W.Z. Li, R.S. Vennila, S.K. Saxena, D.Z. Wang, "Synthesis, microstructure and optical characterization of zirconium oxide nanostructures." Ceramica International 35 (2009)2401–2408.

[55] J. Chen, X. Xiao, Y. Wang, Z. Ye, "Ag nanoparticles decorated WO3/g-C3N4 2D/2D heterostructure with enhanced photocatalytic activity for organic pollutants degradation." Applied Surface Science 467 (2018) 1000–1010.

[56] J. Hu, G. Luo, Z. Li, M. Liu, R. Zou, X. Li, H. Yao, "Deactivation mechanism of KCl and K2SO4 poisoned V2O5/WO3 - TiO2 catalyst on gaseous elemental mercury oxidation." Fuel 278 (2020) 118245.

[57] F. Rinaldi, O. Arutanti, A. Arif, T. Hirano, T. Ogi, K. Okuyama,"Correlations between Reduction Degree and Catalytic Properties of WOx Nanoparticles." ACS Omega 3 (2018) 8963–8970.

[58] R. Gusain, K. Gupta, P. Joshi, O. Khatri, "Adsorptive removal and photocatalytic degradation of organic pollutants using metal oxides and their composites: A comprehensive review." Advances in Colloid and Interface Science 272 (2019) 102009.

[59] D. Hang, K. Sharma, C. Chen, S. Islam, "Enhanced Photocatalytic Performance of ZnO Nanorods Coupled by Two-Dimensional α-MoO3 Nanoflakes under UV and Visible Light Irradiation." Chemistry: A European Journal 22 (2016) 12777–12784.

[60] Y. Liu, X. Xi, Z. Nie, L. Zhao, Y. Fan, "Effect of Hydrothermal Conditions on Crystal Structure, Morphology and Visible-Light Driven Photocatalysis of WO3 Nanostructures." Materials Science Forum 993 (2020) 893–898.

[61] T. Govindaraj, C. Mahendran, R. Marnadu, M. Shkir, V.Manikandan, "The remarkably enhanced visible-light-photocatalytic activity of hydrothermally synthesized WO3 nanorods : An effect of Gd doping." Ceramica International 47 (2021) 4267–4278.